UC Berkeley
UC Berkeley Previously Published Works

Title

Dynamic structural health monitoring of a model wind turbine tower using distributed acoustic sensing (DAS)

Permalink

Journal

ISSN

Authors

Hubbard, Peter G
Xu, James
Zhang, Shenghan
et al.

Publication Date

DOI

Copyright Information

Structural health monitoring of offshore wind turbines using distributed acoustic sensing (DAS)

James T. Xu[1*], Linqing Luo[2], Jaewon Saw[1], Chien-Chih Wang[1], Sumeet K. Sinha[3], Ryan Wolfe[1], Kenichi Soga[1], Yuxin Wu[1], Matthew DeJong[1]

[1*]Department of Civil and Environmental Engineering, University of California Berkeley, Davis Hall, Berkeley, 94720, CA, USA.
[2]Earth and Environmental Sciences, Lawrence Berkeley National Laboratory, Berkeley, 94705, CA, USA.
[3]Department of Civil Engineering, Indian Institute of Technology Delhi, Hauz Khas, New Delhi, 110016, India.

*Corresponding author. E-mail: james.xu@berkeley.edu;

Abstract

This paper presents the results of a first of its kind application and validation of fiber optic strain sensing for structural health monitoring of offshore wind turbines. A full-scale wind turbine was tested at the University of California, Berkeley's shaking table. The test employed two Rayleigh-based Distributed Fiber Optic Sensing (DFOS) technologies to monitor dynamic strain profiles in a wind turbine that was subjected to strains representative of a typical offshore wind turbine environment. The two technologies used were Optical Frequency-Domain Reflectometry (OFDR), which can measure strain (tens of meters), and Phase-sensitive Optical Time-Domain Reflectometry (ϕ-OTDR), a technology used in DAS, which can measure strain over large distances (several kilometers). Target dynamic strain profiles were determined prior to testing using a prototype floating offshore wind turbine simulated in the computational software, OpenFAST. Fiber optic cables were installed onto a wind turbine tower in different orientations to capture global tower deformations and local strain. First, a quasi-static bend test of the entire tower was conducted to calibrate the sensing techniques. Second, the tower was mounted on a six degree of freedom shake table and was subjected to multi-directional (translational and rotational) shaking to induce dynamic strain profiles similar to offshore conditions. Different configurations of loose bolts at the turbine flange connections were also tested to evaluate

1

the proposed sensing approach. The results show good agreement between ϕ-OTDR and OFDR measurements and show that the technologies captured both local and global structural phenomena; the effect of loose bolts on strain response was readily identified. In addition, numerous lessons on effective sensing installation techniques were identified. ϕ-OTDR's ability to accurately capture dynamic strain over large distances makes it a promising candidate for Structural Health Monitoring (SHM) of large civil systems, though mitigating vibration noise is essential to measure small strains accurately.

1 Introduction

Wind turbines are becoming increasingly popular, with 106 gigawatts of onshore wind and 10.8 gigawatts of offshore wind being installed in 2024 worldwide [1]. These wind farms constantly require scheduled inspection and maintenance, which are time-consuming and expensive [2]. Additionally, these scheduled inspections may not find deficiencies, such as loose bolts in the wind turbine tower, which may lead to structural failures [3, 4]. Floating offshore wind turbines, which are used for locations with deep water columns (greater than a few hundred meters), present inherent difficulties in inspection and maintenance due to logistical constraints [5–7]. The scale of onshore and offshore wind farms requires sensing technologies with long-distance capabilities. The vibration frequencies induced by wind turbines also necessitate sensing technologies with high sampling rates. Additionally, popular system identification methods such as Fourier Domain Decomposition (FDD) [8] and covariance-driven Stochastic Subspace Identification method (SSI-COV) [9], estimate modal parameters and shapes from data; sensing higher modes requires high frequency data and finer spatial resolution in the sensor. It is also important for the technology to maintain signal integrity in high-strain rate environments. Distributed Fiber Optic Sensing (DFOS) technologies provides a potential solution. One such technique that satisfies the needs previously mentioned is Phase-sensitive Optical Time-Domain Reflectometry (ϕ-OTDR), which falls within the family of Distributed Acoustic Sensing (DAS) technologies. ϕ-OTDR is particularly well suited to monitor wind farms due to its sensing range (tens of km), high sampling frequency (tens of kHz), and relatively small spatial resolution of channel readouts (1 meter) with a gauge length that can be as small as 2 meters.

The ϕ-OTDR technique was conceived of and developed during the 1990s [10, 11], originally being used for water column acoustic ranging using optical fibers, which led to the method being referred to as DAS [12]. The technique is based on Rayleigh scattering. As light travels along an optical fiber, some of it interacts with inhomogeneities in the fiber and is scattered [13], which is then used to measure a phase change. Although the ϕ-OTDR technique was proposed to monitor dynamic strain early on in its development [11], relatively few applications exist for strain sensing of civil infrastructure [14]. To leverage the advantages associated with ϕ-OTDR in the

context of monitoring offshore and onshore wind farms, the technology should be validated with well-accepted DFOS technologies used in structural health monitoring. Additionally, best practices for data analysis and fiber optic cable installation must be developed to properly interpret the data collected by ϕ-OTDR systems.

A complementary DFOS technology is Optical Frequency-Domain Reflectometry (OFDR), which is similarly based on Rayleigh scattering. OFDR differs from ϕ-OTDR in that the backscattered light is collected in the frequency domain rather than the time domain [14, 15]. OFDR systems have the ability to measure strain at a very fine spatial resolution (less than 1 mm) but have a limited sampling rate (less than 20 Hz) and sensing distance (less than 100 m). OFDR technologies have precedent in monitoring civil infrastructure such as gas pipelines and concrete structures [16–18], but are limited to monitoring low-frequency data for infrastructures that require less than 100 m of sensing distance. This is a drawback for monitoring of large-scale wind farms. However, the OFDR provides useful data for evaluating ϕ-OTDR technologies, and also provides detailed strain information that is useful for laboratory or field testing.

A previous study was conducted that showed that ϕ-OTDR is capable of measuring strain that is comparable to measurements taken using OFDR [19] for small-scale structures experiencing large deformations. This paper expands on evaluating whether ϕ-OTDR is a suitable candidate for monitoring full-scale offshore wind turbines. In this paper, a large-scale turbine tower enables fiber optic cable configurations that are more practical for modern wind turbines, which is vital for downstream tasks. This study investigates the application of ϕ-OTDR for the structural health monitoring (SHM) of floating offshore wind turbines. Floating offshore wind turbines experience different magnitudes and frequencies of loading than of onshore wind turbines. Our research highlights the innovative use of these technologies to measure dynamic strain, which is a critical source of information for assessing the integrity of wind turbine structures in dynamic ocean environments. By focusing on dynamic strain measurement, we aim to provide a more comprehensive understanding of the mechanical strains experienced by offshore wind turbines, which is essential for their maintenance and longevity.

2 Methods

The ideal testing scenario to validate the ability of ϕ-OTDR to measure dynamic strain profiles that are typical of an offshore wind turbine would be to have a functioning offshore wind turbine in a facility that can generate realistic wind, wave, and mooring loads. However, due to typical hub heights of modern offshore wind turbines being around 100 meters and rotor diameters being around 160 meters [20], traditional full-scale testing of offshore wind turbines is not feasible in a laboratory setting. One way to circumvent this issue would be to use hybrid experiments to resolve more complex fluid-structure interaction phenomena. However, this also poses issues when enforcing similitude requirements. The scaling laws necessary to ensure dynamic similitude causes computational bottlenecks in simulation software for a typical design. Moreover, the entire structure (floating substructure, mooring system, tower, blades, etc.) requires fluid-structure interaction simulation. However, since we are primarily

3

concerned with validating the ability of ϕ-OTDR to measure dynamic strain profiles that are typical of an offshore wind turbine, we only require to induce dynamic strain profiles that are in the range of typical strain profiles in both magnitude and frequency.

As a result, this research employed an older full-scale onshore wind turbine, with a scale large enough that any limitations in the spatial resolution of ϕ-OTDR could be evaluated, but not too large to test at the shake table laboratory at UC Berkeley. Dynamic strain profiles of magnitudes and frequency expected for new floating offshore turbines were induced in the older (smaller scale) test specimen using the shake table, as further detailed below. Importantly, the older full-scale turbine still possesses important characteristics (geometry, connections, etc.) required to evaluate monitoring challenges and limitations.

The following subsections provide more details on sensing techniques and the experimental testing procedure.

2.1 OFDR

OFDR data was collected using a Luna Innovations ODiSI6000 commercial OFDR system. The system has four channels, each with the capacity to measure sensing cables of 100-meter length; the measurement frequency can vary in both sampling rate and gauge length. During the four-point bend test, a sampling rate of 1 Hz with a spatial resolution of 2.6 mm was used. During the shake table test, a sampling rate of 2.5 Hz and 5 Hz, with a spatial resolution of 2.6 mm was used. This commercial system has limitations regarding the strain rate when the power of the backscattered light in the frequency domain is uncertain. When the strain rate is high, either temporally or spatially, the readings at those locations become unreliable, limiting the accuracy of dynamic strain profiles. It has less measurement precision than ϕ-OTDR [19, 21], but it can measure strain after periods of signal loss since it measures absolute strain relative to a baseline strain reading.

2.2 ϕ-OTDR

ϕ-OTDR technologies fundamentally measure the optical phase change, $\Delta\phi$, with units of radians of the light wave. The incident wavelength, λ, used in Rayleigh backscattering measurements is around 1550 nm. ϕ-OTDR data was collected using an OptaSense ODH4 interrogator. The interrogator can achieve a sampling rate of up to 200 kHz. Additionally, the maximum length of strain measurement using ϕ-OTDR is 10 km, allowing for large-scale structural health monitoring using only one interrogator. ϕ-OTDR is intended for acoustic sensing in high-frequency dynamic strain environments. One limitation of ϕ-OTDR is that the measured phase change cannot exceed a certain limit. This is detailed in Appendix D. During the four-point bend test, a sampling rate of 1 Hz with a gauge length of 2 meters and a readout spacing of 1 meter were used. During the shake table test, a sampling rate of 4 kHz was used to record strain. A gauge length of 2 meters and a readout spacing of 1 meter were again used.

2.2.1 ϕ-OTDR for dynamic strain monitoring

To convert the phase change measurement to a strain measurement, Equation 1 can be used. The conversion is detailed in Appendix C.

$$\varepsilon = \frac{\lambda}{4\pi n l_g \xi} \Delta \phi \tag{1}$$

In this study, typical values of Pockels coefficients ($p_{11} = 0.126$, $p_{12} = 0.270$) and Poisson's ratio for silica glass ($\nu = 0.17$) [22] were used. The fiber optic cables used had an effective index of refraction of $n = 1.468200$ as specified by the manufacturer. The incident wavelength was taken to be $\lambda = 1550$ nanometers. The gauge length, which is dependent on the interrogator unit used, was $l_g = 2.0419046$ meters. It is important to note that the gauge length represents the fiber length over which the measurements are averaged, corresponding to the effective sensor length over which the average strain is estimated. That is, the gauge length is analogous to the order of the moving average filter [23]. Intuitively, a longer gauge length corresponds to greater spatial averaging [24]; the gauge length controls the spatial resolution and the signal-to-noise ratio [25]. The scale factor, ξ, is defined as a function of n, ν, p_{11}, and p_{12}, and is given by Equation 2.

$$\xi = 1 - \frac{n^2}{2} \left[\nu(p_{11} + p_{12}) + p_{12} \right] \tag{2}$$

2.3 Experiment setup

2.3.1 Experimental specimen

The strain gauge length of the ϕ-OTDR system used in the experiment has a minimum of approximately two meters. Therefore, the spatial scale of the experiment should be as close to a typical offshore wind turbine as possible to match a realistic ratio between the lengths of the strain gauges and structure. A 65-kW Nordtank wind turbine, was used for the experiment. The tower is composed of three separate parts: a bottom section, a middle section, and a top section, all varying in diameter. The bottom and middle sections have a tapered portion that transitions to a smaller diameter. The blades were not attached in this experiment. The turbine properties are listed in Table 1 and the overall dimensions are displayed in Figure 1. A previous study had used another 65-kW Nordtank wind turbine at the Network for Earthquake Engineering Simulation (NEES) shake table [26].
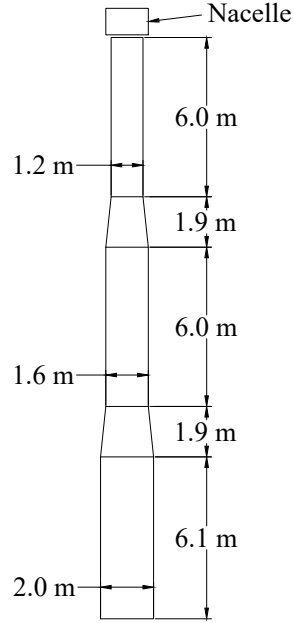
Fig. 1: Elevation view of experimental specimen used with dimensions.

Table 1: Properties of the Nordtank 65-kW wind turbine.

Property	Value
Tower height	21.9 meters
Bottom section length	8.0 meters
Middle section length	7.9 meters
Top section length	6.0 meters
Bottom section diameter	2.0 meters
Middle section diameter	1.6 meters
Top section diameter	1.2 meters
Height to rotor hub center	22.6 meters
Tower thickness	6 millimeters
Young's modulus	191 GPa
Bottom section mass	2885 kg
Middle section mass	2100 kg
Top section mass	1415 kg
Total tower mass	6400 kg
Nacelle mass	2770 kg
Additional mass in nacelle	907 kg
Number of bolts per flange	30 bolts

This particular turbine also has stiffeners between all bolts on both sides of the flanges, shown in more detail in Figure 3b, to prevent local failure mechanisms of the tower.

2.3.2 Fiber optic cable layout

The fiber optic cables were oriented longitudinally along the tower's height, and circumferentially just above and below the flange connections. The layout of the cables for the four-point bend and shake table test are shown in Figures 2a and 2b, respectively. Note that the four-point bend test only included the bottom two tower sections, while the shake table test included all three tower sections.

(a) Four-point bend test. (b) Shake table test.
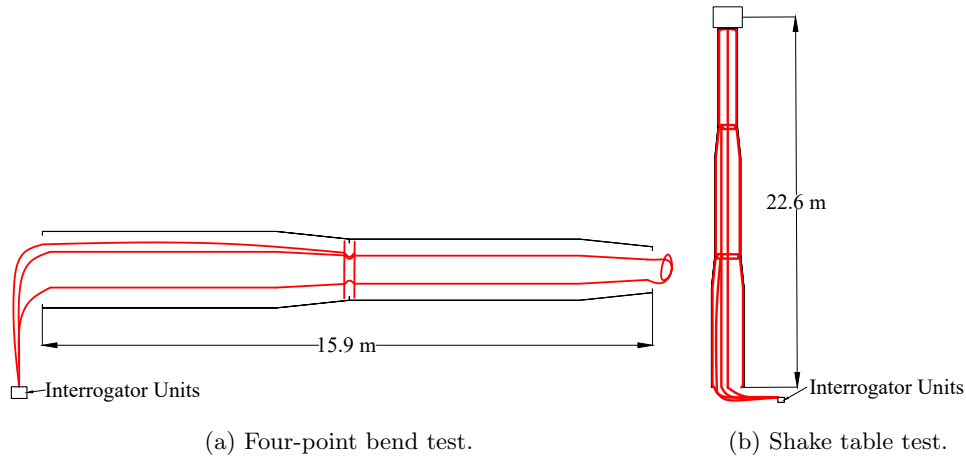
Fig. 2: Fiber optic installation layout (in red) for the four-point bend and shake table test (side views).

The cables that were oriented along the tower's height 'jump' the flanges to continue along the same axis, as shown in Figure 3. Since epoxying the cables directly along the geometry of the turbine tower at the flange would cause issues in the bending radius of the fiber optic cable, the portions of the cable near the flanges were not epoxied to the turbine tower and were slack. This allows for the cable to transverse or 'jump' the flange. The non-epoxied cable length at the flanges is roughly 0.4 meters, centered at the flanges. The cables were secured at the flange so that they would not hit the flange during the shake table test to reduce vibration noise and measurement errors. The circumferential cables were oriented just below and above the flange, approximately 5 centimeters below where the stiffeners ended.

7
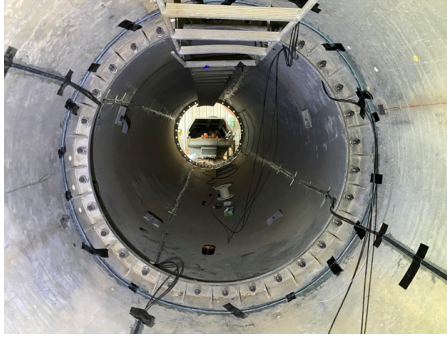
(a) View from the inside of the turbine tower looking down the tower during the four-point bend test.

(b) Close-up of fiber optic cables jumping the flange and the stiffeners at the flanges.

Fig. 3: Black cables are the optical fiber sensing cables.

2.4 Determination of loads using computational models

To determine the appropriate loading to induce typical dynamic strain profiles, two computational tools, Open-source FAST (OpenFAST) and Open System for Earthquake Engineering Simulation (OpenSees), were used. OpenFAST is an open-source multi-physics, multi-fidelity tool for simulating the nonlinear coupled dynamic response of wind turbines, developed by the National Renewable Energy Laboratory (NREL). OpenFAST couples computational modules (aerodynamics, hydrodynamics, structural dynamics, etc.) [27]. The framework builds upon Fatigue, Aerodynamics, Structures, and Turbulence (FAST), its predecessor. The computational tool can also simulate realistic loading conditions, such as stochastic wind fields, using modules like Turbsim. OpenFAST's module relating to the computational modeling of the turbine tower can be used to simulate dynamic strains for realistic loading environments. OpenFAST was used to simulate the structural response experienced by the prototype tower induced by typical loading sources such as wind and wave loadings. To determine typical strain profiles that would be induced in a realistic floating offshore wind turbine tower, a prototype offshore wind turbine, and site location were selected. This prototype configuration was NREL's 5-MW reference wind turbine for offshore system development. This model was used due to its extensive computational validation by NREL and its design which has been adopted for existing floating offshore wind turbines [28, 29]. Humboldt and Morro Bay were chosen as prototype sites due to their potential for future offshore wind farms [30]. The average wave heights, periods, and wind speeds were chosen using the information submitted by the Scripps Institution of Oceanography and NREL [30, 31]. This information was used to create realistic loading conditions. The response was then used to inform the shake table motions used in the experiment.

OpenSees is a finite element modeling framework for simulating the dynamic response of structural and geotechnical systems that was initially developed for

research in earthquake engineering at the Pacific Earthquake Engineering Research (PEER) center [32]. OpenSees was used to model and simulate the Nordtank wind turbine under shake table motions to simulate and confirm that the expected dynamic strain profiles were similar to those experienced by the prototype model simulated using OpenFAST. The Nordtank wind turbine tower was modeled as 50 beam-column elements, with ten beam-column elements in each of the non-tapered and tapered tower sections. The elements were assigned properties (e.g., flexural stiffness, weight) determined by the cross-section at their respective midpoints.

2.5 Four-point bend test

First, to compare the performance of ϕ-OTDR and OFDR under a quasi-static load test, a four-point bend test was conducted. This allowed for a better understanding of the capabilities of the two Rayleigh-based techniques under quasi-static loading and of the local strain field around the circumference of the tower at its connections, for varying bolt configurations. The bottom two sections were connected in the fully bolted configuration and then supported by two cranes to provide a simply supported beam configuration. The tower segment was then loaded symmetrically about the center connection, both 2.9 meters from the center connection to the center of the load along the height of the turbine tower. The load was provided by weights that were loaded onto two pallets which were hanging from the tower section by steel cables. The steel cables were placed on top of wooden struts (with dimensions of 2 inches (5 cm) x 6 inches (10 cm) x 5 feet (1.5 m)) to help distribute the load as evenly as possible, as shown in Figure 4a. The wooden struts were uniformly spaced at 14 inches (35.6 cm), center to center. The steel cables were placed 6 inches from the edge of the wooden strut. Lead weights weighing 500 lbf were placed onto each pallet via a forklift as shown in 4b.
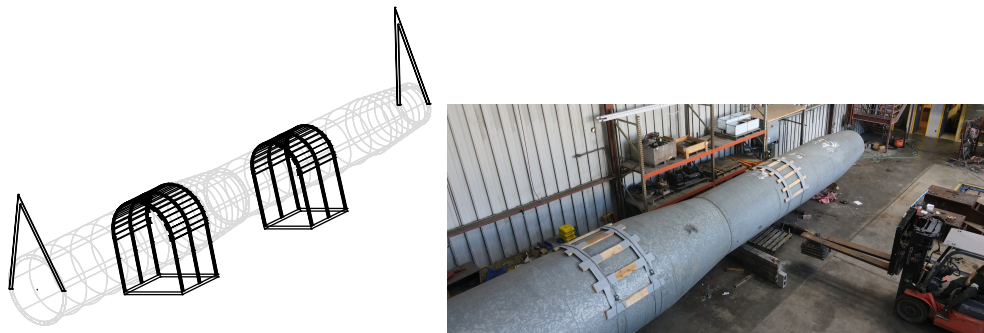
(a) Full view of the bend test configuration with the supports and loading set-up shown in black.

(b) Turbine being loaded with weights.

Fig. 4: Bend test experiment set-up.

Weights totaling 4,000 lbf (2,000 lbf on each pallet) were applied. After placing the weights on the pallets, dynamic vibrations were allowed to decay. Then, a single 500 lbf weight was removed from each pallet, resulting in a total of 3000 lbf. This process was repeated until the pallets had no lead weights. The loading configurations are summarized in Table 2. Measurements were taken throughout the entire duration of the bend test with no interruptions.

Subsequently, a single bolt was fully loosened, resulting in bolt configuration 2. The same loading process was repeated. The previous loose bolt was then torqued and another bolt was fully loosened. This process was repeated until four different bolt configurations, which are shown in Figure 6a, were tested. The naming convention of the cables and the direction of bending are defined in Figure 5. During the entirety of the four-point bend test, the ϕ-OTDR and OFDR interrogators continuously collected data.

Table 2: Four-point bend test loading configurations used for each bolt configuration.

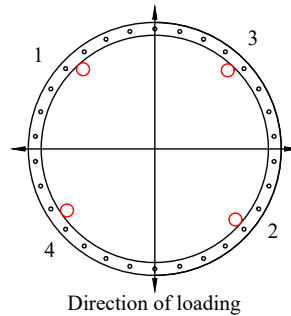| Loading configuration	Total Weight
1	4000 lbf (17793 N)
2	3000 lbf (13345 N)
3	2000 lbf (8896 N)
4	1000 lbf (4448 N)
5	0 lbf (0 N)

Fig. 5: Cross section of turbine tower at the flange, looking up the turbine tower. The red circles indicate the location of the longitudinal fiber optic cables as well as their naming conventions (Axes 1-4).
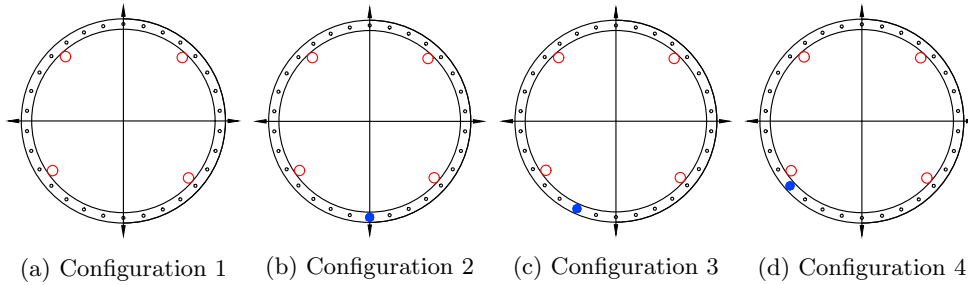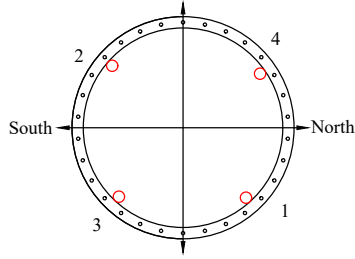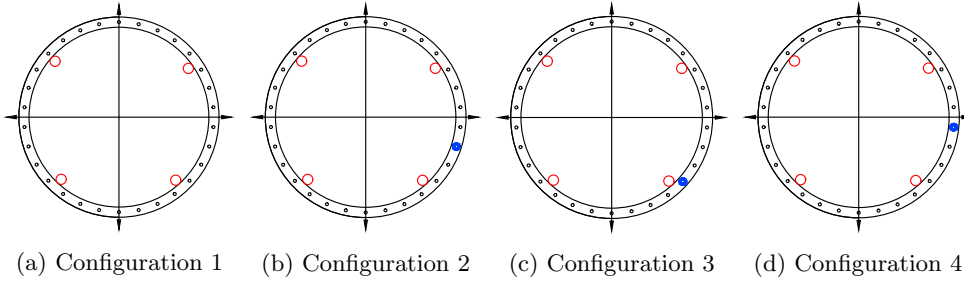
(a) Configuration 1   (b) Configuration 2   (c) Configuration 3   (d) Configuration 4

Fig. 6: Four-point bend test bolt configurations looking up the tower. The figure shows the flange and bolt pattern with the same axis configuration as shown in Figure 5, shown as blue circles around the loose bolt, and red circles indicating the position of the longitudinal cables.

2.6 Shake table test

All three tower segments and the nacelle with additional weight were connected and placed onto the base plate, which was then placed onto the 6-DOF shake table at the PEER center as shown in Figure 7a - 7c. From the results of the OpenFAST simulations of the prototype floating offshore wind turbine and the OpenSees simulations of the Nordtank wind turbine tower, the frequency of strains desired was determined to be around 0.5 Hz for wave loading, and near static (0.05 Hz) for wind loading. A sinusoidal motion at 0.05 Hz that would generate a response with a large enough magnitude would require a large stroke, which would not be feasible due to the limited stroke of the shake table (± 5 inches (± 12.7 cm)). However, to represent the response due to a steady wind condition, an additional weight of 2000 lbf (8896 N) was placed in the nacelle, approximately 2 meters off-center, to represent a steady wind loading. Additionally, a loading configuration tilted the turbine in the south direction to induce additional static load. This was done to make the loading configuration as realistic as possible. The turbine tower was then subjected to three different loading configurations, summarized in Table 3. The configurations were a sinusoidal horizontal ground acceleration with a frequency of 0.5 Hz and an amplitude of 4.8 inches, a sinusoidal horizontal ground acceleration with a frequency of 0.5 Hz and an amplitude of 4.8 inches with a 0.8 degree tilt towards the south direction, and a sinusoidal pure rotation about the base of the tower with an amplitude of 0.8 degrees and frequency of 0.5 Hz. All loading configurations were repeated for each bolt configuration as shown in Figure 9. The naming convention of the cables and the direction of shaking (North-South) are defined in Figure 8. The shake table test occurred over the span of two days. The tests for bolt configurations 1 and 2 were conducted on the first day, and the rest of the tests for the remaining bolt configurations were conducted on the second day. During each day, the ϕ-OTDR and OFDR interrogators continuously collected data.

11

(a) View from the base. (b) Aerial view at time = 0s. (c) Aerial view at time = 1s.

Fig. 7: Wind turbine positioned on the shake table. Figures 7b and 7c show the wind turbine during rotational shaking, with the vertical red line added as a reference.

Table 3: Shake table test loading configurations used for each bolt configuration.

Loading configuration	Loading description	Frequency	Amplitude
1	North-South translational sinusoidal shaking	0.5 Hz	4.8 inches (12.2 cm)
2	North-South translational sinusoidal shaking with tilt	0.5 Hz	4.8 inches (12.2 cm)
3	North-South rotational sinusoidal shaking	0.5 Hz	0.8 degrees

Fig. 8: Cross section of turbine tower at the flange, looking up the turbine tower. The red circles indicate the location of the longitudinal fiber optic cables as well as their naming conventions (Axes 1-4).

(a) Configuration 1   (b) Configuration 2   (c) Configuration 3   (d) Configuration 4

Fig. 9: Shake table test bolt configurations looking up the tower. The figure shows the flange and bolt pattern with the same major axes as shown in Figure 8, with blue circles around the loose bolt, and red circles indicating the position of the longitudinal cables.

3 Results

3.1 Four-point bend test

Due to the loading process during the four-point bend test, the initial loading step of 4000 lbf caused phase determination errors in the ϕ-OTDR data as described in Appendix D. This leads to difficulty comparing different bolt configurations. However, a comparison between the initial loading configuration of 4000 lbf and subsequent loading configurations could be made due to the smaller magnitude of the difference between the loading increments. Some minor phase determination errors during the loading process affected some sensors near the pallets that carried the loading, most likely due to the local vibrational noise caused by the forklift (e.g., vibrations caused by inadvertent collisions between the forklift and turbine tower). However, all minor phase determination errors were corrected for, and all ϕ-OTDR data presented did not have any phase determination errors. Although the OFDR system experiences signal loss during high frequency and magnitude vibrations, the system does not suffer

13

from phase determination errors. It can return strain data relative to its original baseline measurement, which was taken at the beginning of the experiment. Therefore, comparison is possible across all bolt configurations in this test.

During the four-point bend test, there was a temperature increase of roughly 2 degrees Celsius due to the PEER center not being a temperature-controlled environment. The effect of the temperature increase was seen in both the ϕ-OTDR and OFDR data. Since the nature of the loading during the bend test was sudden and caused strain changes orders of magnitudes larger than strain changes due to temperature over the time interval of loading, the data could be separated to remove sudden jumps in the data. The separation process separated the low-frequency drift due to diurnal temperature changes, from the high-frequency phenomenon due to the loading. This was done numerically by accumulating the strains that were less than the jumps in strain due to the sudden loading of the turbine. This isolates the strain due to temperature increase for both ϕ-OTDR and OFDR. The strain change due to temperature increase was subtracted from the original dataset to remove this effect. It is important to note that the OFDR data had an order of magnitude higher noise than ϕ-OTDR data due to the OFDR system's inherent sensor noise ($\pm 5\mu\varepsilon$). Due to the sensor noise, the OFDR data was smoothed using a running average over 15 seconds of data. The loading process for each load step occurred over the span of 2-3 seconds, while the strain induced by temperature was much more gradual, as shown in Figure 10; thus, the running average was chosen to be taken over 15 seconds. The smoothed OFDR strain data was then separated into temperature-induced strains and strains due to loading configurations. All plots of ϕ-OTDR and OFDR measurements show the strain changes due only to the loading configurations. There is a slight dispersion of the sensors due to temperature variations along the length of the cable. In this paper, parameters, such as the choice of the size of the running average window, used in data cleaning and processing were perturbed to ensure the stability of the data cleaning and processing results [33, 34].
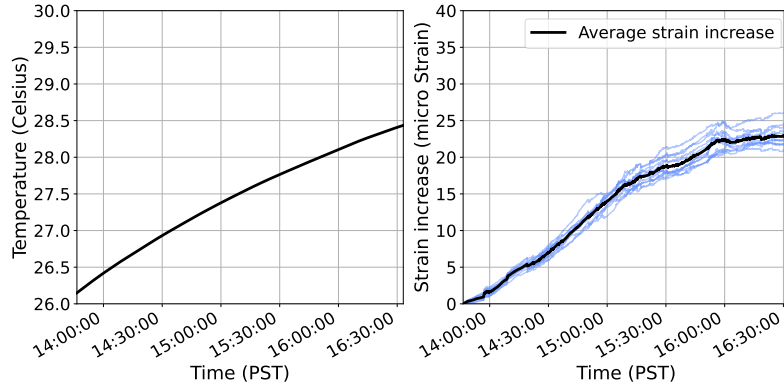

Fig. 10: Increase in temperature and temperature-induced strain during the bend test. In the right-hand plot, each blue line is a sensor, while the black line is the average of the individual sensors.

Figures 11 and 12 show the comparisons between ϕ-OTDR and OFDR strain measurements under all load configurations for a particular bolt configuration. The measurements are zeroed with respect to the final loading configuration of 0 lbf of their respective bolt configuration. Figure 11 shows the theoretical strain assuming idealized simply supported boundary conditions, idealized uniformly distributed loading, Euler-Bernoulli beam theory assumptions, a simple tube cross-section that varies in diameter, and ignores the complexities of the connection of the flanges. The Young's modulus and Poisson's ratio of the turbine was taken to be 191 GPa (27,700 ksi) and 0.3, respectively [26]. ϕ-OTDR and OFDR are generally in good agreement, and display a similar scaling up of recorded strain to that of the theoretical strain. Figure 11 shows that the measurements have the same shape as the expected bending strain distribution. While axes 1 and 2 are similar in shape and magnitude, axes 3 and 4 show a sharp decrease in magnitude near the flange connection. This decrease in axial strain may be due to the fiber optic cables associated with axes 3 and 4 being aligned with the stiffeners, resulting in a greater bending stiffness locally. Additionally, at the connection, the flanges were not in uniform contact with each other, which caused deviations from the theoretical values. The ϕ-OTDR and OFDR measurements are in good agreement, which may indicate that it is the true strain. The other bolt configuration results can be found in Figures A1 - A3.
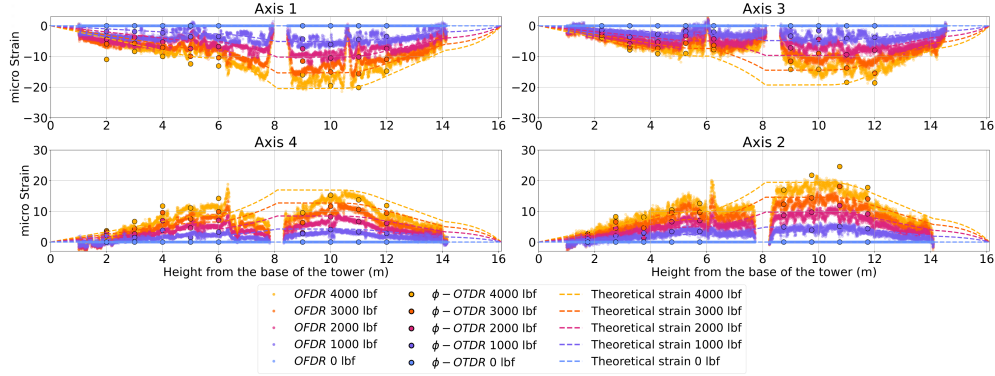

Fig. 11: Axial strain for bolt configuration 1 with theoretical strains plotted.

Figure 12 compares the ϕ-OTDR and OFDR measurements of bolt configuration 1 for the circumferential loops above and below the flange for all load configurations. The other bolt configurations' plots can be found in Figures A4 - A6. For all circumferential plots, the direction of the loading is in the direction from 90 to 270 degrees. There are several peaks in the strain profile that repeat in both the top and bottom loops. This may be due to stress concentrations due to the local stiffeners at the flanges. Figure 12c shows the expected behavior of the hoop strain due to the Poisson effect. Namely, as the loading increased, the hoop strain plot shifted towards the opposite direction of the loading. Due to the spatial resolution of ϕ-OTDR, the peaks are not as apparent but still show the correct behavior in strain differences due to the Poison effect. We

note that around 210 degrees, the ϕ-OTDR measurements differ due to part of the gauge length of that sensor point not being epoxied from the tower.
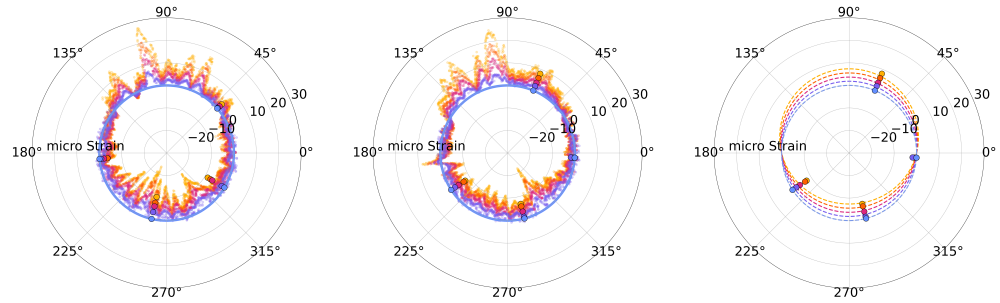

(a) ϕ-OTDR and OFDR data of circumferential loop just below the flange.

(b) ϕ-OTDR and OFDR data of circumferential loop just above the flange.

(c) Comparison of circumferential loop ϕ-OTDR data and theoretical hoop strain.

Fig. 12: Circumferential strain comparison for bolt configuration 1, looking up the tower. See Figure 11 for legend.

As previously mentioned, due to ϕ-OTDR's issue with phase determination errors, which is problematic when the nature of the loading is step-like, which was the case during the four-point bend test, comparisons between different bolt configurations become difficult due to this vibration noise. On the other hand, OFDR does not suffer from phase determination errors, which allows for comparisons between different bolt configurations. Figure 13 shows the comparison of OFDR across all bolt configurations for their respective 0 lbf load configuration strain profiles. For each bolt configuration, the strain profile is zeroed out with respect to bolt configuration 1's strain profile, which is why Figure 13a is a circle at 0 $\mu\varepsilon$. In Figures 13b - 13d, there is a clear large increase in the hoop strain at the locations of the bolts that were loosened at each bolt configuration, even under the self-weight of the turbine, before applying the weights.
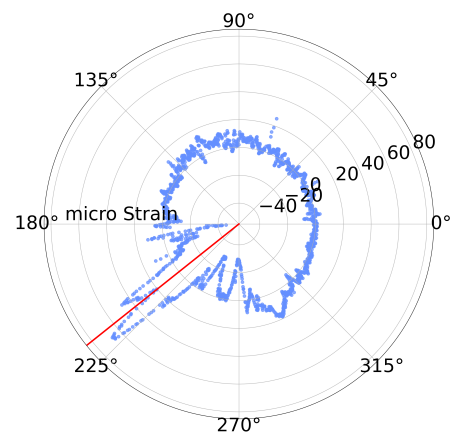
16
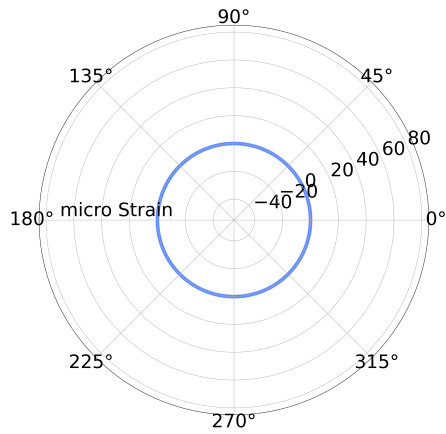
(a) Bolt configuration 1.
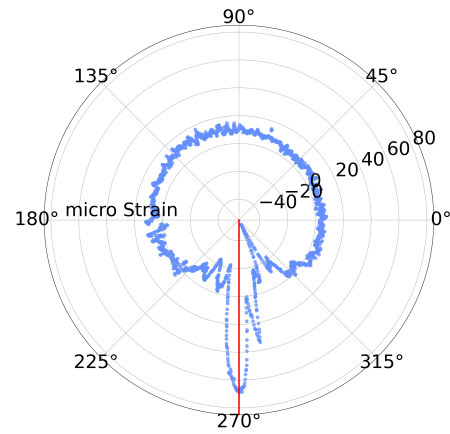
(b) Bolt configuration 2.
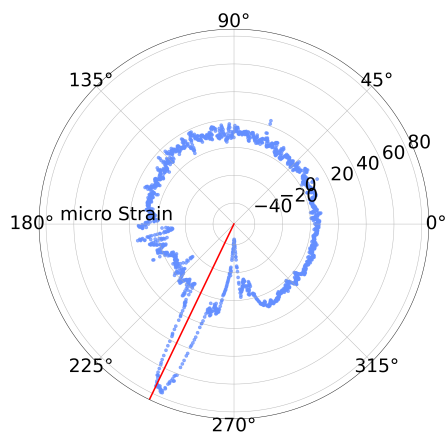
(c) Bolt configuration 3.

(d) Bolt configuration 4.

Fig. 13: Circumferential strain for all bolt configurations zeroed out from bolt configuration 1 at 0 lbf loading, looking up the tower. The red lines indicate the location of the loose bolt.

3.2 Shake table test

During the shake table test, OFDR experienced severe signal loss due to the high strain rate environment during the duration of shaking. The experimental specimen was excited with high-frequency noise vibrations due to the shake table's imperfect feedback. Due to signal loss of OFDR, a comparison between the maximum and minimum strains for each load configuration measured by OFDR and ϕ-OTDR was made. The comparison of the minimum and maximum strain envelopes for bolt configuration 1 is shown in Figure 14. The other bolt configurations are shown in Figures B7 -

17

B9. This was done to validate the magnitude of the strain measured by ϕ-OTDR. It should be noted that due to the signal loss of the OFDR system, several of the minimum and maximum values of the sensors underestimate the magnitudes of the true strain. This behavior can be seen in Figures 14, and B7 - B9, where several of the minimum and maximum values of the OFDR measurements are dispersed (shown as the blue dots). Axis 1 and axis 2 were comprised of a single fiber optic cable, and axis 4 and axis 3 were comprised of a separate single fiber optic cable. At the bottom of the tower, axes 1 and 4 were directly connected to the OFDR system, which resulted in less signal loss in those axes. The dispersion of the minimum and maximum OFDR strain values due to signal loss grows nearly linearly along the sensing distance. Additionally, there was generally more signal loss for higher strain rates. For example, for the translational shaking, which induced a smaller strain response than the rotational shaking, the minimum and maximum OFDR strain values are more concentrated in Figure 14's load configuration 1 than the strain envelopes in Figure 14's load configuration 3. This can be attributed to more signal loss for bolt configuration 3. To make a better comparison between the OFDR and ϕ-OTDR, the strain envelopes of the OFDR data were determined by finding the local extrema of the minimum and maximum strain values and taking the running average of these values. A window size of 5 was used to find the extrema and a running average was shown to effectively extract the true OFDR strain envelope. Comparing the strain envelope profiles, it is observed that there is good agreement, with ϕ-OTDR profiles matching the OFDR profiles. Due to the bottom segment of Axis 4 having lower OFDR signal loss than the other segments, the mean percent error of the strain envelope thickness was computed against the ϕ-OTDR strain envelope thickness. The OFDR strain envelope values used for comparison were computed using the spatial average of strain envelope values over the corresponding ϕ-OTDR gauge length. This allows for a direct comparison between the OFDR and ϕ-OTDR strain envelopes. For Figure 11, the mean percent errors for load configurations 1, 2, and 3 were 10.1%, 10.2%, and 13.4%, respectively. The discrepancy was partly due to the signal loss experienced as the loading magnitude increased and the imperfect strain envelope from the OFDR data.
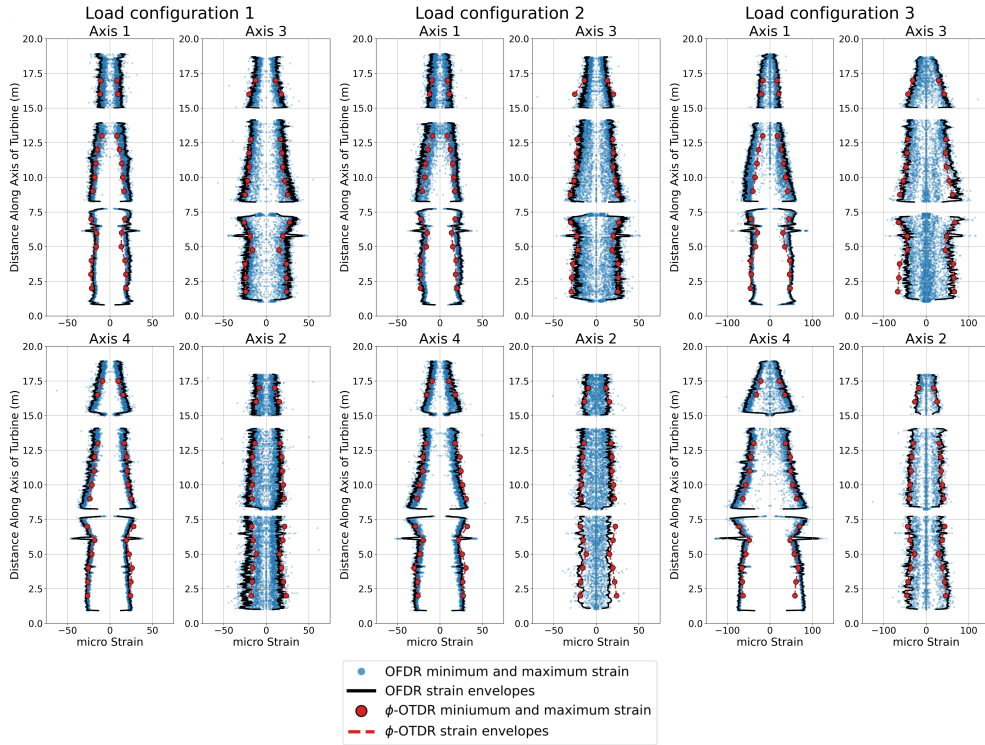
Fig. 14: Strain envelope comparisons for bolt configuration 1.

Figure 15 shows the strain time series measured by ϕ-OTDR. The response of the two south-most axes (2 and 3) and the response of the two north-most axes (1 and 4) have a similar amplitude and are 180 degrees out of phase, i.e., when the south-most axes experience a tensile (positive) strain, the north-most axes experience a similar magnitude compressive (negative) strain, as expected.
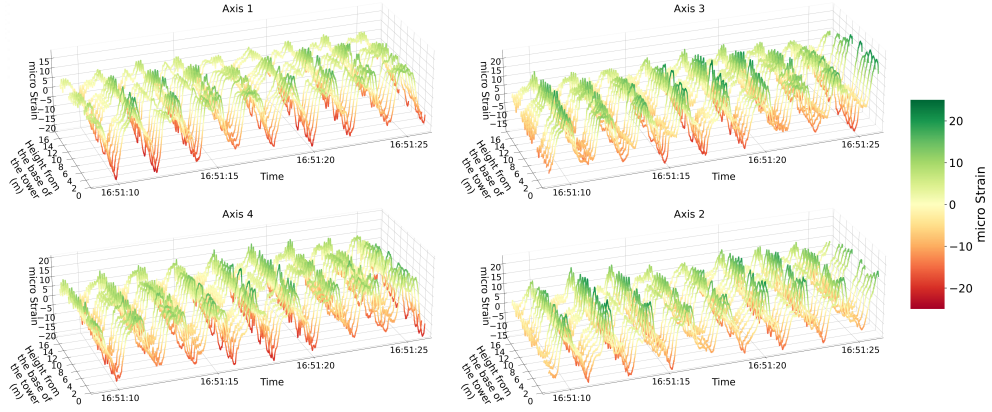
19

Fig. 15: ϕ-OTDR strain time series during the translational loading configuration for bolt configuration 1.

3.2.1 Frequency and modal information captured by ϕ-OTDR

Figure 16 shows the averaged power spectral densities of all the sensors in the bottom section of axis 3 of the ϕ-OTDR sensors during the translational shaking at 0.5 Hz. The power spectral densities were calculated after applying a high-pass filter with a cutoff frequency of 0.15 Hz. The forcing frequency at 0.5 Hz is clearly identified, and there are also peaks at integer multiples of 0.5 Hz (harmonics) due to the shake table loading. There is also a peak that corresponds with the natural frequency of the turbine, occurring around 1.4 Hz. The natural frequencies of the bolt configurations were identified in Table 4.
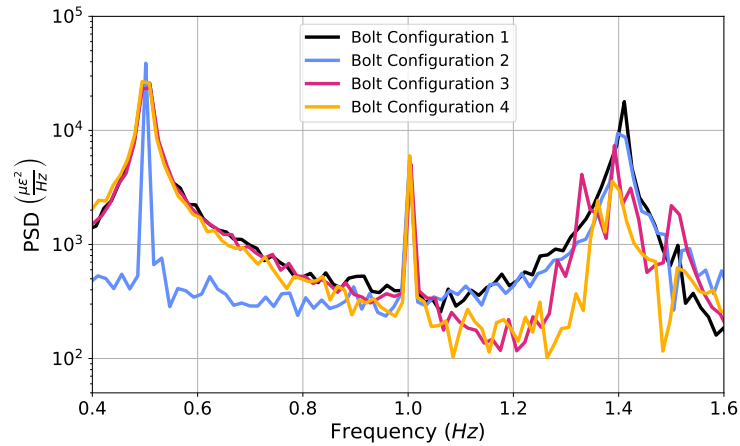

Fig. 16: Averaged PSD values for the longitudinal channels in the bottom section of axis 3 using ϕ-OTDR data during the translational shaking with tilt.

20

Table 4: Shake test averaged PSD's for each bolt configuration during loading configuration 2.

Bolt configuration	Identified natural frequency
1	1.411 Hz
2	1.398 Hz
3	1.392 Hz
4	1.388 Hz

4 Discussion

Regarding the shake table test results, all results were zeroed from the beginning of each shaking phase. In Figure 14, we generally observe good agreement between OFDR and ϕ-OTDR measurements for the minimum and the maximum strain values. Since the sampling frequency of the OFDR and ϕ-OTDR for the longitudinal cables during the shake test was 2.5 Hz and 4 kHz, respectively, and the total run was only 60 seconds with a forcing frequency of approximately 0.5 Hz, there may be some discrepancy between the two measurements. Due to OFDR's low sampling rate, the maximum and minimum values may underestimate the true magnitude of maximum and minimum strains. Additionally, some strain values may not be correct due to the limitation of the high strain rate, as mentioned in Section 2, which may result in an overestimation of the strain. Some discrepancies from the ϕ-OTDR measurements may again be due to the large gauge length and further acoustic noise.

Another important aspect of fiber optic sensing is the installation of the cables themselves. When instrumenting the structure with fiber optic cable, the epoxy should be applied evenly so that the fiber optic cable is fully adhered to the structure. This ensures that the phase changes in the fiber optic cables are due to the structure undergoing strain and not to the debonding of the fiber optic cable from the structure. As the epoxy cures, it is essential to hold the fiber optic cables in the desired configuration. Regarding Section 2.2.1, it is worth noting that the precision of ε is dependent on the precision of the coefficients ν, p_{11}, p_{12}, and n.

Due to sources of error such as laser frequency drift, temperature-induced refractive index changes, and incorrect phase determination, ϕ-OTDR data must be properly post-processed and interpreted. Laser drift and diurnal temperature changes tend to occur at low frequencies. A high-pass filter can be implemented to isolate the structural response due to higher frequency loadings. As previously mentioned, in this study a high-pass filter with a cutoff frequency of 0.15 Hz was used to remove low-frequency strain changes due to temperature and laser drift. Consequently, the effect of the tilt of the turbine tower and eccentric loading in the nacelle is not apparent after filtering. It is important to note that if the structure has natural frequencies of interest below 0.15 Hz, applying a high-pass filter would remove the information related to those natural frequencies. However, recent advancements have allowed for measuring static loadings [35], which would allow for the detection of low-frequency loadings.

5 Conclusion

In this study, the ϕ-OTDR technique was validated against an industry-accepted OFDR system for the structural health monitoring of wind turbines. The two technologies were compared for both a four-point bend test and a shake table test. While OFDR has a high spatial resolution, it could not capture high-frequency information due to its limited sampling rate. Additionally, signal loss was found to occur in high strain-rate environments, which are associated with high-frequency vibrations. ϕ-OTDR was found to have no signal loss and was able to accurately capture the dynamic response of a wind turbine that underwent a shake table test. It was found that ϕ-OTDR was also able to capture frequency information and changes in the modal properties of the structure, which is necessary for applications of ϕ-OTDR data for system identification methods. ϕ-OTDR is a promising technology for the SHM of offshore wind turbines due to its high sensing distance and high sampling rate, and has been shown in this study to provide accurate measurements of dynamic strain profiles. Due to the high sensing distance, ϕ-OTDR has the capability of monitoring several turbines with a single fiber optic cable while providing a relatively high spatial resolution which is also essential. Additionally, the high sampling rate allows for the detection of higher modes which are not currently possible with OFDR technologies.

Data availability

All datasets supporting this study's findings are available from the National Science Foundation NaturalHazards Engineering Research Infrastructure DesignSafe Data Depot: PRJ-5735. https://doi.org/10.17603/ds2-2qkc-3q70 [36].

References

[1] Lee, J., Zhao, F.: Global Wind Report 2024

[2] Márquez, F.P.G., Tobias, A.M., Pérez, J.M.P., Papaelias, M.: Condition monitoring of wind turbines: Techniques and methods. Renewable energy **46**, 169–178 (2012)

[3] Xianlong, H., Tianli, S.: A new identification method for bolt looseness in wind turbine towers. Shock and Vibration **2019**(1), 6056181 (2019)

[4] Ma, Y., Martinez-Vazquez, P., Baniotopoulos, C.: Wind turbine tower collapse cases: A historical overview. Proceedings of the Institution of Civil Engineers-Structures and Buildings **172**(8), 547–555 (2019)

[5] Maples, B., et al.: Installation, Operation, and Maintenance Strategies to Reduce the Cost of Offshore Wind Energy vol. NREL/TP-5000-57403

[6] Gonzalo, A.P., Benmessaoud, T., Entezami, M., Márquez, F.P.G.: Optimal maintenance management of offshore wind turbines by minimizing the costs. Sustainable Energy Technologies and Assessments **52**, 102230 (2022)

[7] Dos Reis, M.M.L., Mazetto, B.M., Da Silva, E.C.M.: Economic analysis for implantation of an offshore wind farm in the brazilian coast. Sustainable Energy Technologies and Assessments **43**, 100955 (2021)

[8] Brincker, R., Zhang, L., Andersen, P.: Modal identification from ambient responses using frequency domain decomposition. In: IMAC 18: Proceedings of the International Modal Analysis Conference (IMAC), San Antonio, Texas, USA, February 7-10, 2000, pp. 625–630 (2000)

[9] Magalhães, F., Cunha, A., Caetano, E.: Online automatic identification of the modal parameters of a long span arch bridge. Mechanical Systems and Signal Processing **23**(2), 316–329 (2009)

[10] Dakin, J., Lamb, C.: A sensing method employing a fibre optic sensor system. Int. Appl (1991)

[11] Posey Jr, R., Johnson, G., Vohra, S.: Strain sensing based on coherent rayleigh scattering in an optical fibre. Electronics Letters **36**(20), 1 (2000)

[12] Lindsey, N.J.: Fiber-optic seismology in theory and practice. PhD thesis, University of California, Berkeley (2019)

[13] Bao, X., Wang, Y.: Recent advancements in rayleigh scattering-based distributed fiber sensors. Advanced Devices Instrumentation **2021**, 1–17 (2021) https://doi.org/10.34133/2021/8696571

[14] Hubbard, P.G.: Monitoring distributed, dynamic strain in civil infrastructure using phase-sensitive optical time-domain reflectometry. PhD thesis, University of California, Berkeley (2022)

[15] Ding, Z., Wang, C., Liu, K., Jiang, J., Yang, D., Pan, G., Pu, Z., Liu, T.: Distributed optical fiber sensors based on optical frequency domain reflectometry: A review. Sensors **18**(4), 1072 (2018)

[16] Bado, M.F., Casas, J.R., Barrias, A.: Performance of rayleigh-based distributed optical fiber sensors bonded to reinforcing bars in bending. Sensors **18**(9), 3125 (2018)

[17] Bado, M.F., Casas, J.R.: A review of recent distributed optical fiber sensors applications for civil engineering structural health monitoring. Sensors **21**(5), 1818 (2021)

[18] Ren, L., Jiang, T., Jia, Z.-g., Li, D.-s., Yuan, C.-l., Li, H.-n.: Pipeline corrosion and leakage monitoring based on the distributed optical fiber sensing technology. Measurement **122**, 57–65 (2018)

[19] Hubbard, P.G., *et al.*: Dynamic structural health monitoring of a model

wind turbine tower using distributed acoustic sensing (das). Journal of Civil Structural Health Monitoring **11**, 833–849 (2021) https://doi.org/10.1007/s13349-021-00483-y

[20] Stehly, T., Duffy, P.: 2020 Cost of Wind Energy Review. Technical Report NREL/TP-5000-81209, National Renewable Energy Laboratory, Golden, Colorado (January 2022)

[21] Sasaki, T., Zhang, S., Soga, K., Luo, L., Freifeld, B., Kitayama, Y., Kawaguchi, K., Sugiyama, H.: Distributed fiber optic strain sensing of bending deformation of a well mockup in the laboratory. Journal of Natural Gas Science and Engineering **96**, 104309 (2021)

[22] Giallorenzi, T.G., Sigel, G.H., Bucaro, J.A.: Optical fiber sensor technology. In: Proceedings of the Optical Fiber Communication Conference, vol. 18, pp. 626–665 (1982). https://doi.org/10.1364/OFC.1982.ThGG1 . Optical Society of America

[23] Näsholm, S.P., Iranpour, K., Wuestefeld, A., Dando, B.D., Baird, A.F., Oye, V.: Array signal processing on distributed acoustic sensing data: Directivity effects in slowness space. Journal of Geophysical Research: Solid Earth **127**(2), 2021–023587 (2022)

[24] Vantassel, J.P., Cox, B.R., Hubbard, P.G., Yust, M.: Extracting high-resolution, multi-mode surface wave dispersion data from distributed acoustic sensing measurements using the multichannel analysis of surface waves. arXiv preprint arXiv:2202.04779 (2022)

[25] Paitz, P., Edme, P., Schmelzbach, C., Doetsch, J., Gräff, D., Walter, F., Lindsey, N., Chalari, A., Fichtner, A.: Distributed acoustic sensing from mhz to khz: Empirical investigations of das instrument response. In: EGU General Assembly Conference Abstracts, p. 7343 (2020)

[26] Prowell, I.: An experimental and numerical study of wind turbine seismic behavior. PhD thesis, University of California, San Diego (2011)

[27] Jonkman, J.: OpenFAST Documentation, Release 1.0 (2017)

[28] Jonkman, J., et al.: Definition of a 5-MW Reference Wind Turbine for Offshore System Development. Technical Report NREL/TP-500-38060, National Renewable Energy Laboratory, Golden, Colorado (February 2009)

[29] Office, W.E.T.: Offshore Wind Market Report 2022. https://www.energy.gov/eere/wind/articles/offshore-wind-market-report-2022-edition (2022)

[30] Bodini, N., et al.: Update on nrel's 2020 offshore wind resource assessment for the california pacific outer continental shelf. Technical report, National Renewable Energy Laboratory (NREL), Golden, CO (United States) (2022)

[31] Commerce, N.O., Administration, A.: NDBC Station Page. https://www.ndbc.noaa.gov/station_page.php?station=46244 (2022)

[32] Mazzoni, S., *et al.*: Opensees command language manual. Pacific Earthquake Engineering Research (PEER) Center **264**(1), 137–158 (2006)

[33] Yu, B.: Veridical data science. In: Proceedings of the 13th International Conference on Web Search and Data Mining, pp. 4–5 (2020)

[34] Yu, B., Barter, R.L.: Veridical Data Science: The Practice of Responsible Data Analysis and Decision Making. MIT Press, Cambridge, MA (2024)

[35] Crickmore, R., Ku, E.: Fibre optic distributed sensing. Google Patents. US Patent 10,247,584 (2019)

[36] Xu, J., Luo, L., Saw, J., Wang, C.C., Sinha, S., Wolfe, R., Soga, K., Wu, Y., DeJong, M.: Fiber optic monitoring of offshore wind turbines using OFDR and Phi-OTDR technologies. Designsafe-CI (2024). https://doi.org/10.17603/DS2-2QKC-3Q70 . https://www.designsafe-ci.org/data/browser/public/designsafe.storage.published/PRJ-5735/#detail-4f381854-b596-42c2-8997-b2b459fcd09c

[37] Grattan, K., Meggitt, B.: Optical Fiber Sensor Technology: Advanced applications-Bragg Gratings and Distributed Sensors vol. 5. Springer, New York, NY (2000)

[38] SEAFOM Fiber Optic Monitoring Group: Measuring sensor performance document - 02. Technical Report SEAFOM MSP-02, IOP Publishing, United Kingdom (2018)

[39] Pockels, F.: Ueber die durch einseitigen druck hervorgerufene doppelbrechung regulärer krystalle, speciell von steinsalz und sylvin. Annalen der Physik **275**(3), 440–469 (1890) https://doi.org/10.1002/andp.18902750313

[40] Hughes, R., Jarzynski, J.: Static pressure sensitivity amplification in interferometric fiber-optic hydrophones. Applied Optics **19**(1), 98–107 (1980) https://doi.org/10.1364/AO.19.000098

[41] Schroeder, J.: Brillouin scattering and pockels coefficients in silicate glasses. Journal of Non-Crystalline Solids **40**(1), 549–566 (1980) https://doi.org/10.1016/0022-3093(80)90129-5

[42] Hartog, A.H.: An Introduction to Distributed Optical Fibre Sensors. CRC press, Boca Raton, FL (2017)

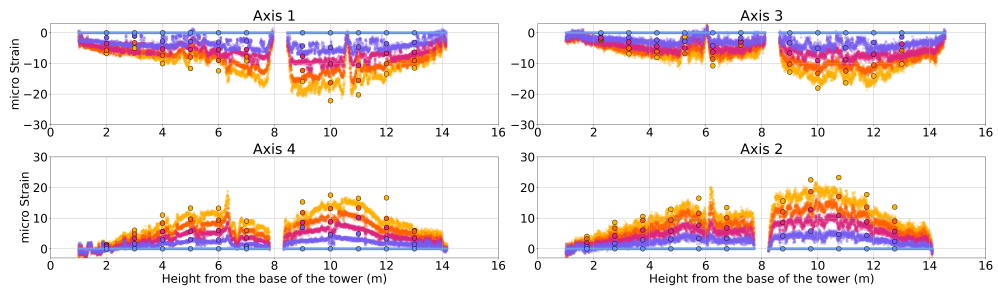# Appendix A Additional results from the four-point bend test

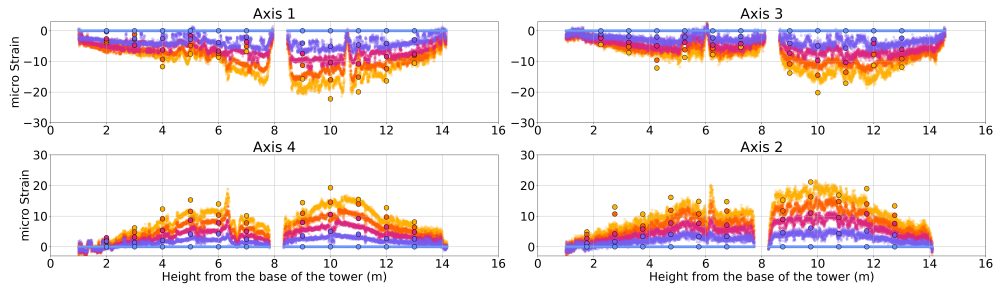**Fig. A1**: Axial strain for bolt configuration 2. See Figure 11 for legend.

Fig. A2: Axial strain for bolt configuration 3. See Figure 11 for legend.
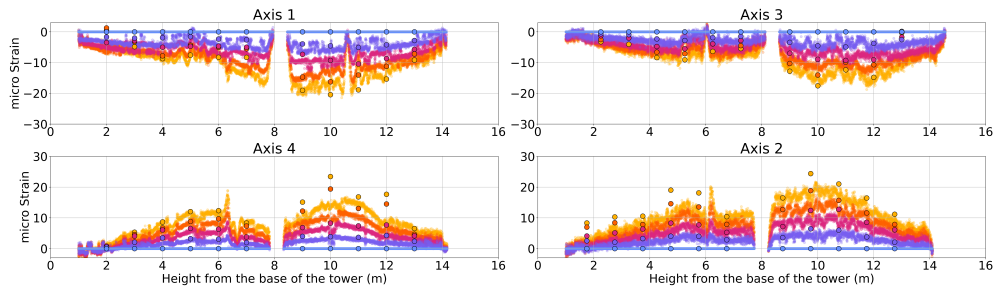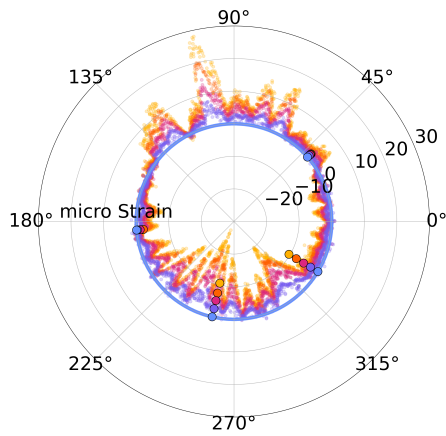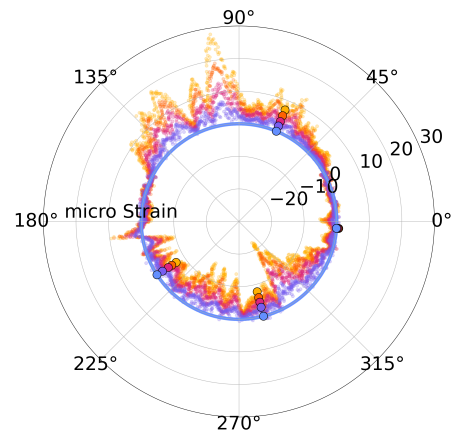

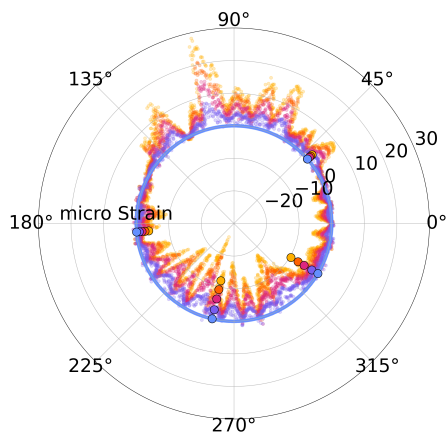**Fig. A3**: Axial strain for bolt configuration 4. See Figure 11 for legend.
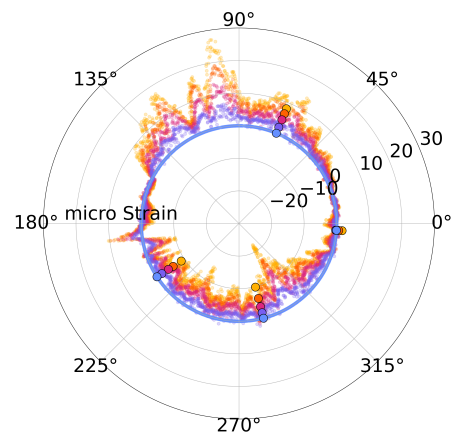
(a) Circumferential loop just below the flange.

(b) Circumferential loop just above the flange.

Fig. A4: Circumferential strain comparison for bolt configuration 2, looking up the tower. See Figure 11 for legend.
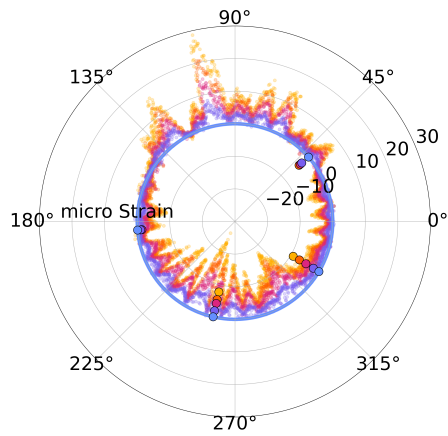

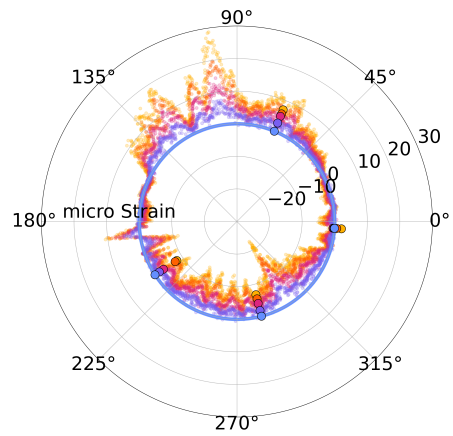(a) Circumferential loop just below the flange.

(b) Circumferential loop just above the flange.

Fig. A5: Circumferential strain comparison for bolt configuration 3, looking up the tower. See Figure 11 for legend.
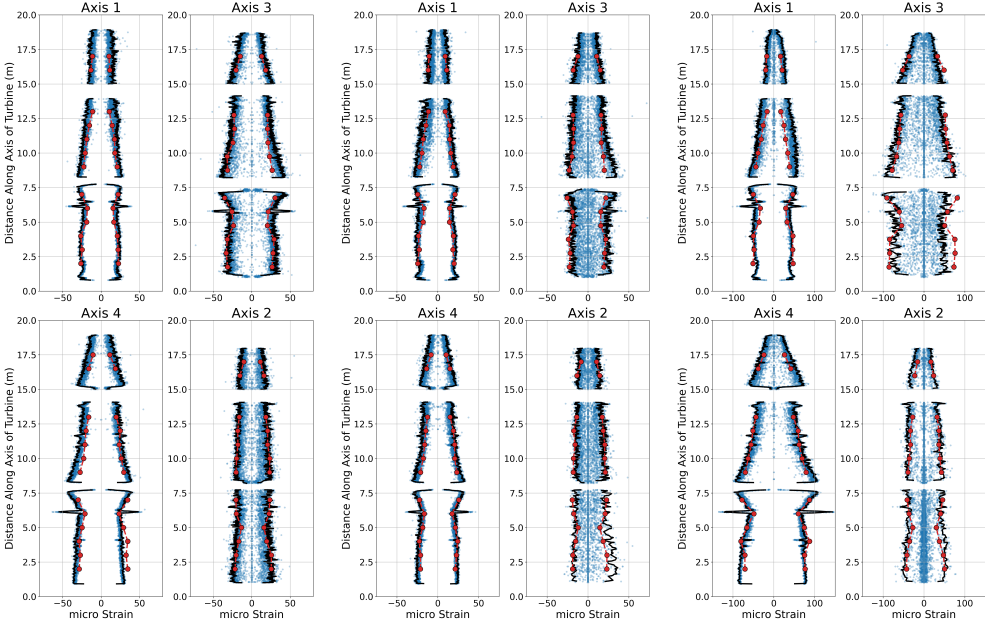
(a) Circumferential loop just below the flange.

(b) Circumferential loop just above the flange.

Fig. A6: Circumferential strain comparison for bolt configuration 3, looking up the tower. See Figure 11 for legend.
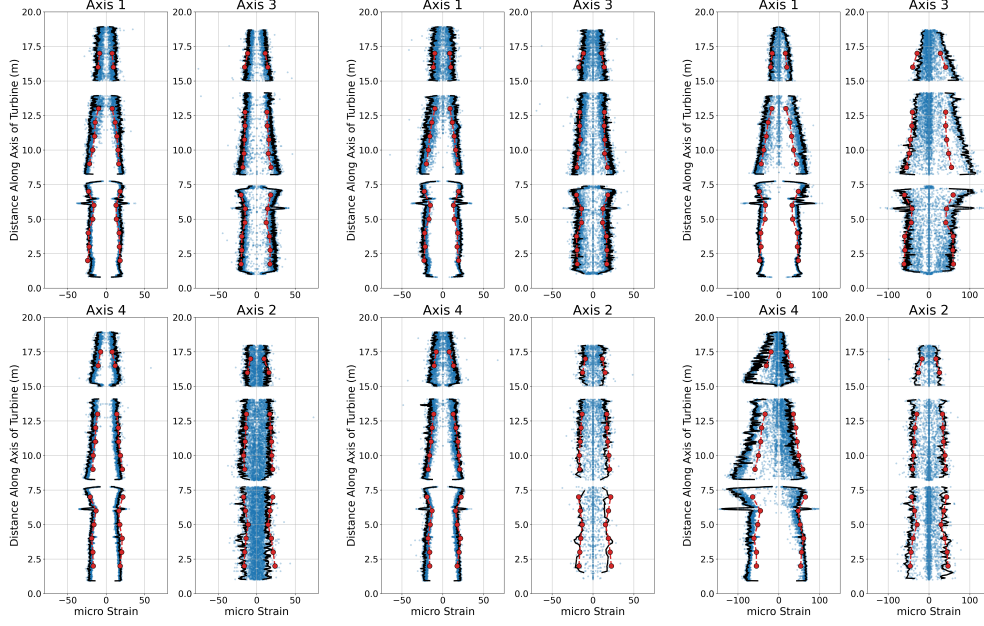
Appendix B Additional results from the shake table test

(a) Loading configuration 1.   (b) Loading configuration 2.   (c) Loading configuration 3.

Fig. B7: Strain envelope comparisons for bolt configuration 2. See Figure 14 for legend.
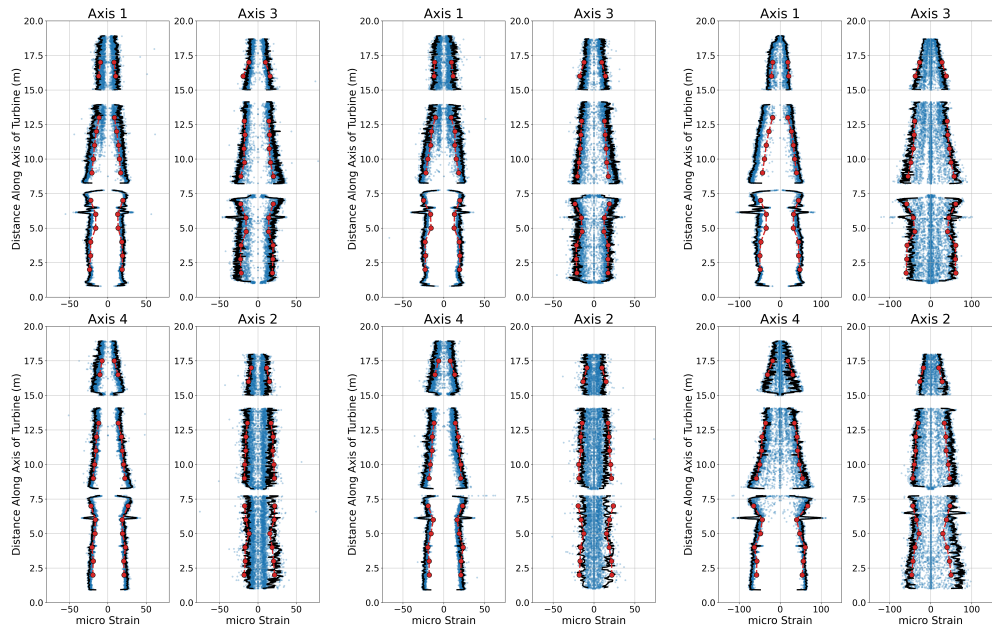
(a) Loading configuration 1. (b) Loading configuration 2. (c) Loading configuration 3.

Fig. B8: Strain envelope comparisons for bolt configuration 3. See Figure 14 for legend.

(a) Loading configuration 1. (b) Loading configuration 2. (c) Loading configuration 3.

Fig. B9: Strain envelope comparisons for bolt configuration 4. See Figure 14 for legend.

Appendix C   Phase to strain conversion details

Since the fundamental measurement of ϕ-OTDR is the optical phase change, the quantity must be converted to strain. The conversion is covered in detail in this section. The phase change divided by the unaltered light phase, $\frac{\Delta\phi}{\phi}$, can be expressed as a summation of the length of fiber change (i.e., axial strain, ε along the fiber, $\frac{\Delta l}{l} = \varepsilon$), effective refractive index change, $\frac{\Delta n}{n}$, and optical wavelength change, $\frac{\Delta\lambda}{\lambda}$, as follows [37, 38]:

$$\frac{\Delta\phi}{\phi} = \frac{\Delta l}{l} + \frac{\Delta n}{n} + \frac{\Delta\lambda}{\lambda} \tag{C1}$$

The effective index of refraction is dependent on strain due to the photoelastic effect, also known as Pockels effect [39]; a relationship between the effective refractive index and axial strain is needed. This can be described using Poisson's ratio, ν, of the fiber, and the Pockels coefficients, p_{11}, p_{12} [40], [41]:

$$\frac{\Delta n}{n} = -\frac{n^2}{2}\left[\nu(p_{11} + p_{12})\frac{\Delta l}{l} + p_{12}\frac{\Delta l}{l}\right] \tag{C2}$$

31

Assuming that optical dispersion is negligible $\left(i.e. \frac{\Delta\lambda}{\lambda} = 0\right)$ since Rayleigh backscattering measurements are made at the incident wavelength [12] gives:

$$
\begin{aligned}
\frac{\Delta\phi}{\phi} &= \frac{\Delta l}{l} - \frac{n^2}{2}\left[\nu(p_{11} + p_{12})\frac{\Delta l}{l} + p_{12}\frac{\Delta l}{l}\right] \\
&= \xi\frac{\Delta l}{l}
\end{aligned}
\tag{C3}
$$

where the scale factor, ξ, is defined as a function of n, ν, p_{11}, and p_{12}:

$$
\xi = 1 - \frac{n^2}{2}\left[\nu(p_{11} + p_{12}) + p_{12}\right]
\tag{C4}
$$

To calculate the unaltered light phase over the gauge length of optical fiber, l_g, for two-way transit, the following relation [14, 38] can be used:

$$
\phi = \frac{4\pi n l_g}{\lambda}
\tag{C5}
$$

The relationship between strain and measured optical phase change is obtained by substituting Equation C5 into Equation C3:

$$
\Delta\phi = \xi\frac{\Delta l}{l}\phi
\tag{C6}
$$

$$
\implies \frac{\Delta l}{l} = \varepsilon = \frac{\lambda}{4\pi n l_g \xi}\Delta\phi
\tag{C7}
$$

Appendix D   A note on phase wrapping for ϕ-OTDR

If the measured phase change is greater than $\pm 2\pi$, the signal will remain in the interval $[-\pi, \pi]$ rather than following the true strain value. This can cause errors which are typically characterized by step-like jumps in the recorded phase data. This imposes a restriction on the capability of ϕ-OTDR to accurately measure phase changes, which is inversely proportional to the frequency of the true signal [42]. The maximum phase change rate, $\Delta\dot{\phi}_{max}$, that can be measured is given by [14]:

$$
\Delta\dot{\phi}_{max} = \pi f_N
\tag{D8}
$$

Due to uncertainty in phase determination, the signal may need to be unwrapped before further analysis. However, it is important to note that if the nature of the loading causes a high enough phase change rate, unwrapping the signal can be challenging and may lead to removing the actual physical strain measured.